



**UNIVERSITY OF LEEDS**

This is a repository copy of *New Global Meteoric Smoke Observations From SOFIE: Insight Regarding Chemical Composition, Meteoric Influx, and Hemispheric Asymmetry*.

White Rose Research Online URL for this paper:  
<https://eprints.whiterose.ac.uk/175897/>

Version: Accepted Version

---

**Article:**

Hervig, ME, Plane, JMC [orcid.org/0000-0003-3648-6893](https://orcid.org/0000-0003-3648-6893), Siskind, DE et al. (3 more authors) (2021) *New Global Meteoric Smoke Observations From SOFIE: Insight Regarding Chemical Composition, Meteoric Influx, and Hemispheric Asymmetry*. *Journal of Geophysical Research: Atmospheres*, 126 (13). e2021JD035007. ISSN 2169-897X

<https://doi.org/10.1029/2021jd035007>

---

**Reuse**

Items deposited in White Rose Research Online are protected by copyright, with all rights reserved unless indicated otherwise. They may be downloaded and/or printed for private study, or other acts as permitted by national copyright laws. The publisher or other rights holders may allow further reproduction and re-use of the full text version. This is indicated by the licence information on the White Rose Research Online record for the item.

**Takedown**

If you consider content in White Rose Research Online to be in breach of UK law, please notify us by emailing [eprints@whiterose.ac.uk](mailto:eprints@whiterose.ac.uk) including the URL of the record and the reason for the withdrawal request.



[eprints@whiterose.ac.uk](mailto:eprints@whiterose.ac.uk)  
<https://eprints.whiterose.ac.uk/>

1 **Meteoric smoke and meteor influx from global SOFIE observations**

2

3 **Mark E. Hervig<sup>1</sup>, John M. C. Plane<sup>2</sup>, Dave E. Siskind<sup>3</sup>, Wuhu Feng<sup>2,4</sup>, Charles G.**  
4 **Bardeen<sup>5</sup>, and Scott M. Bailey<sup>6</sup>.**

5 <sup>1</sup>GATS, Driggs, Idaho, USA.

6 <sup>2</sup>School of Chemistry, University of Leeds, Leeds, UK.

7 <sup>3</sup>Space Science Division, Naval Research Laboratory, Washington, DC, USA.

8 <sup>4</sup>NCAS School of Earth and Environment, University of Leeds, Leeds, UK.

9 <sup>5</sup>National Center for Atmospheric Research, Boulder, Colorado, USA.

10 <sup>6</sup>Virginia Polytechnic Institute, Blacksburg, Virginia, USA.

11 Corresponding author: Mark Hervig (m.e.hervig@gats-inc.com)

12

13 **Main Points:**

14 1) The composition of smoke in the mesosphere is consistent with iron-rich olivine.

15 2) Global ablated meteoric influx is estimated to be  $7.3 \pm 2.0$  metric tons / day, with a total influx  
16 of  $25.0 \pm 7.0$  tons / day.

17 3) Hemispheric asymmetries in smoke and H<sub>2</sub>O are consistent with stronger winter descent in the  
18 Northern polar mesosphere relative to the South.

19

20 **Abstract.** Measurements from the Solar Occultation For Ice Experiment (SOFIE) in both  
21 hemispheres are used to characterize meteoric smoke in the mesosphere and to estimate the  
22 meteoric flux into Earth's atmosphere. New smoke extinction retrievals from sunrise  
23 measurements in the Northern Hemisphere (NH) are presented, which complement the previously  
24 reported sunset observations in the Southern Hemisphere (SH). The sunrise observations are in  
25 good agreement with simulations from the Whole Atmosphere Community Climate Model  
26 (WACCM), for both the seasonal and height dependence of smoke in the mesosphere. The SOFIE  
27 - WACCM comparisons assumed that smoke in the mesosphere exists purely as Fe-rich olivine.  
28 This is justified because olivine is detected optically by SOFIE, meteoric ablation is predicted to  
29 inject similar quantities of the most abundant elements (Fe, Mg and Si) into the mesosphere, and  
30 olivine is anticipated by theory and laboratory experiments. In addition, the ablated and total  
31 meteoric influx determined from SOFIE assuming Fe-rich olivine is in agreement with a recent  
32 and independent investigation based on models and observations. SOFIE observations from 2007  
33 - 2021 indicate a global ablated meteoric influx of  $7.3 \pm 2.0$  metric tons per day ( $\text{t d}^{-1}$ ), which  
34 corresponds to a total influx (ablated plus surviving material) of  $25.0 \pm 7.0 \text{ t d}^{-1}$ . Finally, the results  
35 indicate stronger descent in the NH polar winter mesosphere than in the SH winter. This  
36 hemispheric asymmetry at polar latitudes is indicated by smoke and water vapor results from both  
37 SOFIE and WACCM.

## 38 1. Introduction

39 A layer of meteoric smoke resides in the mesosphere and stratosphere, as nanometer sized  
40 aerosol that results from the ablation of cosmic dust particles during atmospheric entry [*Plane et*  
41 *al.*, 2012; *Hervig et al.*, 2017a]. Smoke in the mesosphere is enhanced during polar winter and  
42 reduced in summer, due to transport by the global meridional mesospheric circulation. This  
43 behavior was first predicted by a two-dimensional model [*Megner et al.*, 2008] and later observed  
44 by the Solar Occultation for Ice Experiment (SOFIE) [*Hervig et al.*, 2009]. The annual variation  
45 in smoke occurs despite the annual variation in meteoric influx (MI), which is highest (lowest)  
46 near the fall (spring) equinox [*Fentzke et al.*, 2008]. The phase difference between smoke in the  
47 middle atmosphere and meteoric influx is due to the dominance of transport in the mesosphere, as  
48 discussed by *Bardeen et al.* [2008].

49 Estimates of the total meteoric influx (TMI, ablated plus surviving material) into Earth's  
50 atmosphere range from 1 to 270 metric tons per day ( $\text{t d}^{-1}$ ) [e.g., *Plane*, 2012]. The most recent  
51 results, however, appear to be converging on a narrower range (30 - 60  $\text{t d}^{-1}$ ) than previously.  
52 *Gardner et al.* [2014] report a TMI of  $60 \pm 16 \text{ t d}^{-1}$  based on mid-latitude lidar observations of  
53 sodium near the mesopause combined with models. *Carrillo-Sánchez et al.* [2016] derived a TMI  
54 of  $43 \pm 14 \text{ t d}^{-1}$  by combining a meteoric ablation model with a solar system dust model, constrained  
55 by lidar measurements of the vertical fluxes of mesospheric Na and Fe at mid-latitudes and cosmic  
56 spherule deposition at the South Pole. Importantly, they also found that only ~18% of the incoming  
57 meteoric material is ablated (and thus resident in the middle atmosphere), far lower than previous  
58 estimates (>80%) [e.g., *Vondrak et al.*, 2008]. *Hervig et al.* [2017a] used SOFIE satellite  
59 observations of meteor smoke in the Southern Hemisphere (SH) mesosphere to derive a TMI of  
60  $30 \pm 18 \text{ t d}^{-1}$ . Most recently, *Carrillo-Sánchez et al.* [2020] report an update to the *Carrillo-Sánchez*

61 *et al.* [2016] analysis (a new chemical ablation model) which suggests  $TMI = 28 \pm 16 \text{ t d}^{-1}$ , and a  
62 slightly higher ablated fraction (30%) than previously.

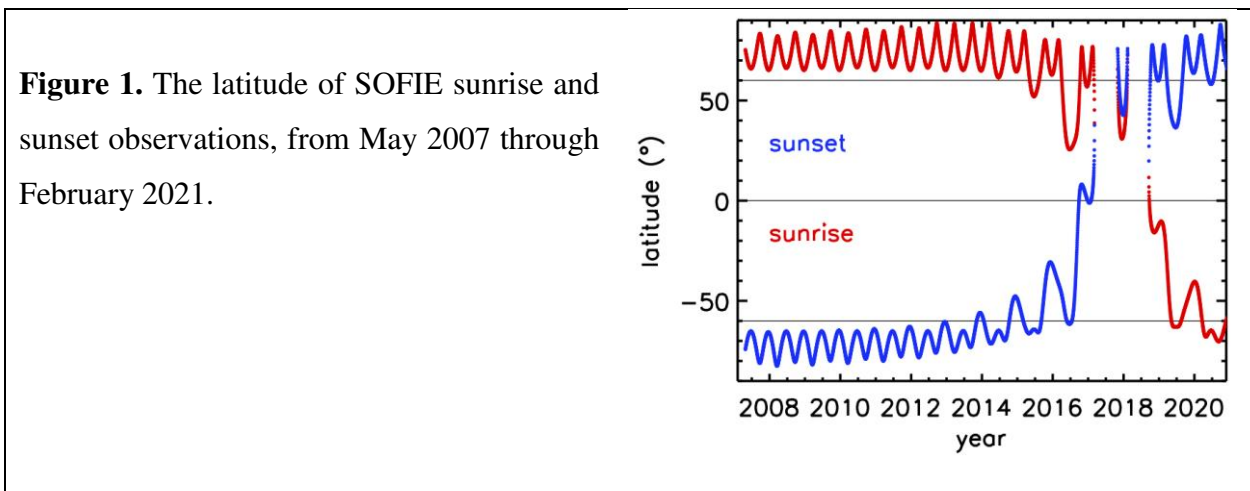
63 The present study uses SOFIE observations to examine the time and height dependence of  
64 meteoric smoke in the Northern Hemisphere (NH), for the first time. This advance comes from  
65 new methods for calibrating the detector response drift during sunrise, which has been more  
66 challenging than for the sunset measurements. The new smoke results are compared to models and  
67 to SOFIE sunset observations, and subsequently used to determine meteoric influx during 2007 -  
68 2021 in both hemispheres.

## 69 **2. SOFIE Observations**

70 SOFIE has observed temperature, five gases ( $O_3$ ,  $H_2O$ ,  $CO_2$ ,  $CH_4$ , and  $NO$ ), polar  
71 mesospheric clouds (PMC), and meteoric smoke, from the Aeronomy of Ice in the Mesosphere  
72 (AIM) satellite during 2007 - present [Russell *et al.*, 2009]. The occultation measurements are used  
73 to conduct retrievals at altitudes from roughly 20 to 95 km (up to 150 km for  $NO$ ), with a vertical  
74 resolution of  $\sim 1.8$  km. The measurement latitudes have evolved over the years, with dedicated  
75 polar coverage from 2007 – 2016 and 2019 – present. The years from 2017 - 2019 had equatorial  
76 coverage with some interruptions, and a change from sunsets (sunrise) in the SH (NH) to the NH  
77 (SH), due to progression of the AIM orbit (Figure 1). The current SOFIE data is version 1.3 which  
78 is available online ([sofie.gats-inc.com](http://sofie.gats-inc.com)).

79 The primary challenge in interpreting the meteoric smoke signals is accounting for a small  
80 drift in detector responsivity, which occurs due to heating of the system during solar view. The  
81 response drift is small ( $< 10$  counts) compared to the dynamic range ( $2^{15}$  counts), but significant  
82 in terms of the response due to meteoric smoke ( $< 20$  counts). For sunset observations the drift is  
83 highly linear, and is successfully removed by extrapolating a fit to measurements above the

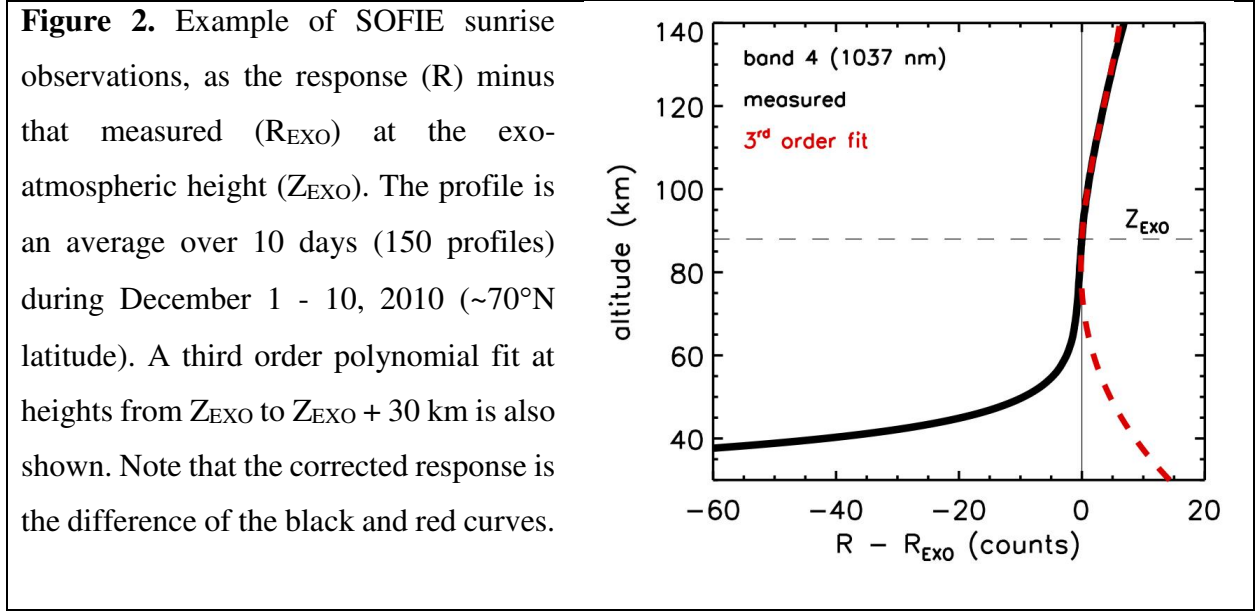
84 atmosphere (exo-atmospheric) to lower heights [Gordley *et al.*, 2009]. Results for sunset smoke  
 85 observations were first described by *Hervig et al.* [2009], who reported smoke extinction ( $\beta(\lambda)$ ) at  
 86 1037 nm wavelength ( $\lambda$ ). An updated response calibration approach [*Hervig et al.*, 2017a]  
 87 provided sunset smoke extinctions at the additional wavelengths of 330 and 867 nm, which  
 88 subsequently allowed the chemical composition of smoke to be identified. Sunset measurements  
 89 benefit from a long period of solar observation above the atmosphere, which allows the instrument  
 90 temperature to achieve a state of steady linear change, facilitating straightforward corrections to  
 91 the signals. The drift in sunrise measurements is more difficult to characterize, however, because  
 92 the atmosphere is observed before the instrument temperature has a chance to stabilize.



93

94 The drift in sunrise observations above the atmosphere was found to be consistent with a  
 95 third order polynomial. Attempting such a high-order fit to individual measurements can be  
 96 problematic, however, as variations due to noise can cause unrealistic values in the subsequent  
 97 extrapolation to atmospheric altitudes. This issue is eliminated when fitting a polynomial to the  
 98 average signal versus height based on multiple days (15 observations per day) as discussed in  
 99 *Hervig et al.* [2017a]. The results here used 10-day averages (150 profiles), as shown in the  
 100 example in Figure 2, where the response (R) minus the exo-atmospheric response ( $R_{EXO}$ ) is shown

101 versus height. This approach was found to reduce the statistical uncertainty in the drift corrections  
 102 to levels that were below both the statistical noise limit ( $\sim 0.3$  counts, see *Gordley et al.*, 2009) and  
 103 the atmospheric response. The uncertainty in retrieved smoke extinction is defined as the root-  
 104 sum-square of the measurement noise, drift correction uncertainty, and errors in removal of  
 105 interference. Interference is due to  $O_3$  absorption and Rayleigh scattering at 330 and 867 nm, and  
 106 only Rayleigh at 1037 nm. As a result the 1037 nm observations have the lowest uncertainties, and  
 107 are thus used here to determine meteoric influx.



108

109 For this work meteoric smoke extinctions were retrieved using 10-day averages of SOFIE  
 110 signals, for observations from 2007 - 2021. The signal averages used only measurements that were  
 111 free of PMCs, which are opaque enough to overwhelm the signal due to smoke. For the new sunrise  
 112 (NH) observations reported here, this results in a lack of smoke extinctions during June and July  
 113 when PMCs are ubiquitous at polar latitudes. Similarly, SH smoke extinctions are rarely obtained  
 114 during December - January.

115           SOFIE measurements of smoke extinction are converted to volume density ( $V$ ) using the  
116 relationship reported by *Hervig et al.* [2017a],  $V = C \beta(1037)$ , where  $C$  is a constant that varies  
117 with smoke composition. This linear relationship exists because at the SOFIE wavelengths smoke  
118 attenuation is entirely due to absorption, which is proportional to the particle radius cubed.  
119 Obtaining estimates of  $V$  from SOFIE allows direct comparison with the models, and also provides  
120 a means to determine meteoric influx. SOFIE multi-wavelength observations show that the most  
121 likely (>60% detection probability) smoke compositions are magnesiowüstite ( $\text{Mg}_x\text{Fe}_{1-x}\text{O}$ ,  $x = 0,$   
122  $0.1, 0.2,$  and  $0.6$ ) and iron-rich olivine ( $\text{Mg}_{0.8}\text{Fe}_{1.2}\text{SiO}_4$ ) [*Hervig et al.*, 2017a]. Note that values of  
123  $C$  span roughly 250 to 1900 ( $\mu\text{m}^3 \text{cm}^{-3} \text{km}$ ) for the potential smoke compositions. Furthermore,  
124 the different smoke compositions can be identified simultaneously in the SOFIE multiwavelength  
125 measurements, due to their spectral similarity combined with SOFIE uncertainties. Of the  
126 compounds indicated by SOFIE, only olivine has an elemental makeup that is similar to the relative  
127 elemental abundances of ablated meteoric material (see Table 1). Furthermore, laboratory and  
128 theoretical studies suggest that iron-rich olivine should result from the recombination of meteoric  
129 ablation products in the mesosphere [*Saunders and Plane*, 2011]. Taking these clues, the SOFIE  
130 extinctions were analyzed below assuming that smoke consists only of  $\text{Mg}_{0.8}\text{Fe}_{1.2}\text{SiO}_4$ . The first  
131 consequence is that the conversion of extinction to volume density becomes  $V/\beta = 1512 \pm 1 \mu\text{m}^3$   
132  $\text{cm}^{-3} \text{km}$ . This is in contrast to the previous interpretation which used the average  $V/\beta$  for the  
133 possible compositions ( $687 \pm 470 \mu\text{m}^3 \text{cm}^{-3} \text{km}$ ), and accepted the large standard deviation as an  
134 experimental uncertainty [*Hervig et al.*, 2017a]. Note that the resulting SOFIE  $V$  (and MI) are  
135 increased here by a factor of  $\sim 2$  compared to previous results that assumed the average optical  
136 properties for a range of smoke compositions. The second consequence of assuming  
137  $\text{Mg}_{0.8}\text{Fe}_{1.2}\text{SiO}_4$  is that the SOFIE ablated influx has an elemental breakdown consistent with that



138 predicted by combining chemical ablation and solar system dust models with observations  
 139 [Carrillo-Sánchez *et al.*, 2020]. This in turn provides a straightforward relationship between the  
 140 ablated meteoric influx determined from SOFIE (see Section 5) and total meteoric influx (ablated  
 141 plus surviving material).

**Table 1.** Relative abundance of the top five meteoric elements, listed for incoming meteoroids, and for the top three smoke compositions identified by SOFIE.

Element	Ablated Influx <sup>1</sup> (t d <sup>-1</sup> )	Influx Fraction <sup>1</sup> (% by wt.)	Olivine <sup>2</sup> Mg <sub>0.8</sub> Fe <sub>1.2</sub> SiO <sub>4</sub> (% by wt.)	Magnesiowüstite <sup>2</sup> Mg <sub>0.6</sub> Fe <sub>0.4</sub> O (% by wt.)	Wüstite <sup>2</sup> FeO (% by wt.)
Fe	2.8	34	38	42	78
O	2.7	32	36	30	22
Si	1.2	14	16	-	-
Mg	1.0	12	11	27	-
Na	0.3	3	-	-	-

<sup>1</sup>According to Carrillo-Sanchez *et al.* [2020].  
<sup>2</sup>Composition identified using SOFIE multiwavelength smoke observations [Hervig *et al.*, 2017a]. The detection probabilities were 68% for olivine, 75% for magnesiowüstite, and 71% for Wüstite.

### 142 3. WACCM Model

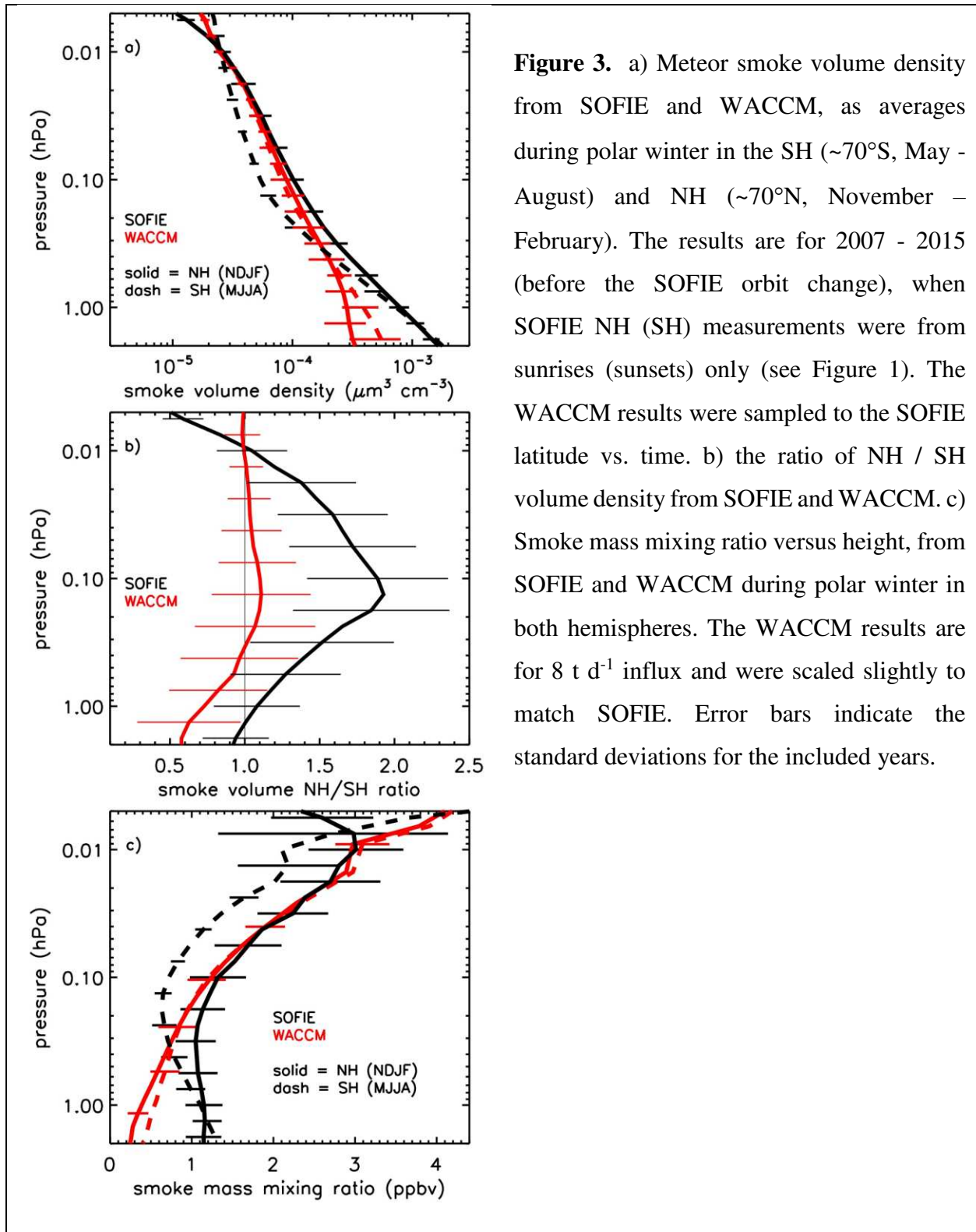
143 This work used a model description of meteoric smoke based on a first principles  
 144 representation in the Whole Atmosphere Community Climate Model (WACCM), as originally  
 145 described by Bardeen *et al.* [2008]. The model begins with meteoric ablation products as metal-  
 146 rich molecular clusters of 0.25 nm radius, and simulates the evolution of smoke particles due to  
 147 growth by agglomeration, sedimentation, and transport. The model includes annual and latitudinal  
 148 variations in meteoric influx [Fentzke *et al.*, 2008], with the ablated meteoric influx (AMI)  
 149 specified as the annual global mean. Note that the model only considers the ablated fraction of  
 150 incoming meteoroids, since the surviving material falls quickly to the surface [Plane *et al.*, 2012].  
 151 Later model adaptations used the original smoke component of Bardeen *et al.* [2008] incorporated  
 152 in the specified dynamics (SD) version of WACCM [Bardeen *et al.*, 2010]. The smoke simulations  
 153 were later integrated into NCAR Community Earth System Model (CESM) version of WACCM

154 [Marsh *et al.*, 2013a; 2013b], along with new descriptions of the gas-phase chemistry of meteoric  
155 metals and interactions between smoke and trace gases [Saunders *et al.*, 2012; Plane *et al.*, 2015;  
156 Frankland *et al.*, 2015; James *et al.*, 2017]. Finally, the model is nudged with the Modern-Era  
157 Retrospective Analysis for Research and Applications (MERRA2) [Molod *et al.*, 2015; Gelaro *et*  
158 *al.*, 2017]. This is the version used here, which is maintained at the University of Leeds, and was  
159 previously used in comparisons with SOFIE by Hervig *et al.* [2017a]. WACCM results for 2007 -  
160 2020 were used here to determine daily zonal means which were sampled to the SOFIE latitude  
161 versus time.

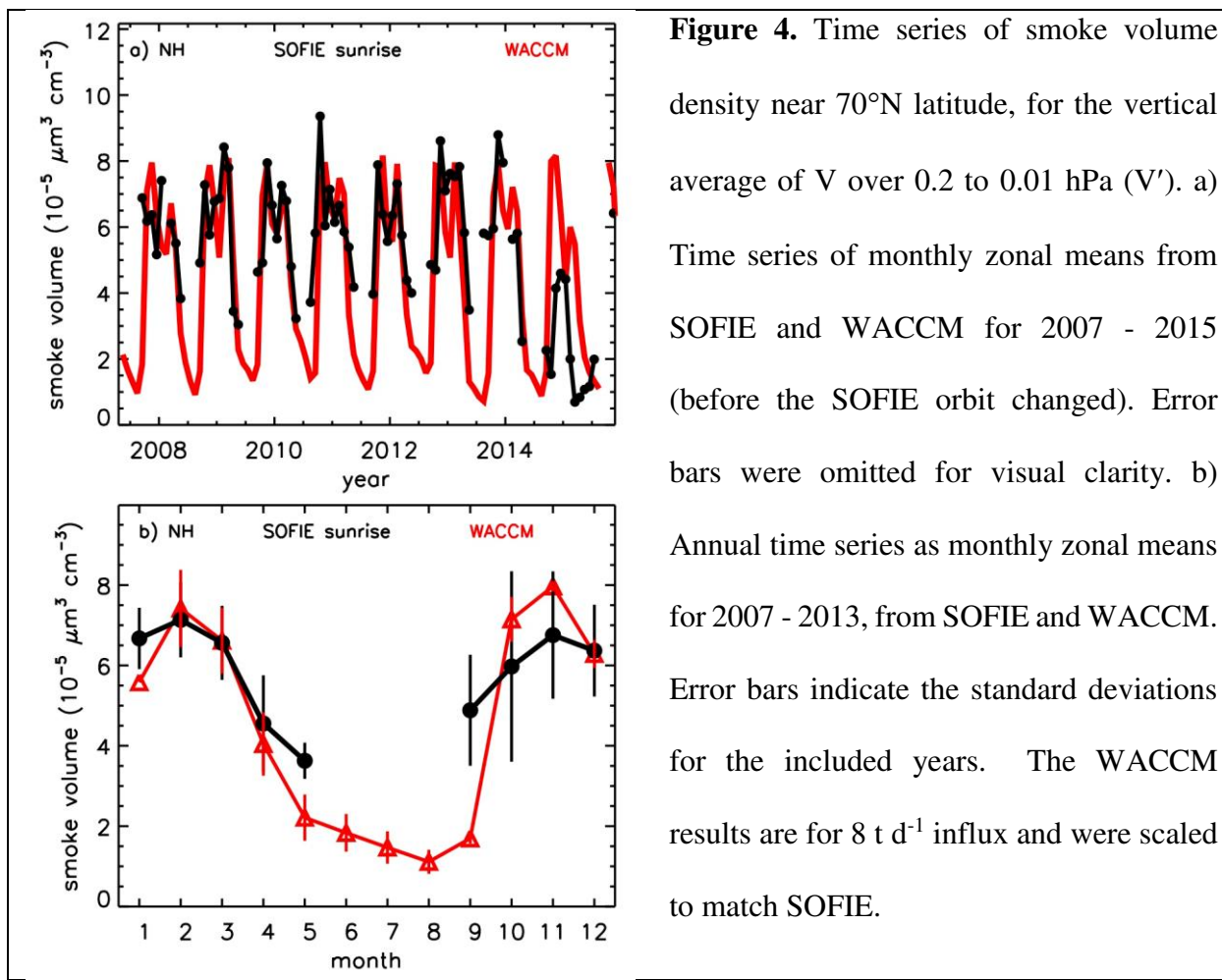
#### 162 **4. Meteoric Smoke**

163 The new SOFIE NH (sunrise) smoke V profiles are compared to SOFIE observations in  
164 the SH (sunset) in Figure 3a, where the results are averages for polar latitudes during winter months  
165 when smoke is highest. The NH and SH V profiles are generally similar; however, note that SOFIE  
166 shows greater smoke volume density in the NH middle mesosphere. Results from WACCM are  
167 also shown in Figure 3a. The WACCM results are for  $8 \text{ t d}^{-1}$ , and were scaled slightly to match  
168 SOFIE (factor of 1.2). Note that this is equivalent to adjusting the ablated influx in the model (see  
169 Section 5 for detail). SOFIE is systematically greater than WACCM in the lower mesosphere ( $P >$   
170  $\sim 0.5 \text{ hPa}$ ). This difference was explored by Hervig *et al.* [2017b], who found that it was consistent  
171 with a layer of neutralized sulfate mixed with smoke at altitudes above the nominal sulfate layer  
172 during autumn - winter, when temperatures are low. SOFIE indicates a larger hemispheric (NH vs.  
173 SH) difference in the middle mesosphere ( $\sim 0.2 - 0.01 \text{ hPa}$ ) than is shown by WACCM. These  
174 differences are further illustrated in Figure 3b, where the NH / SH V ratios are shown versus height.  
175 This rendition shows that SOFIE and WACCM both indicate a similar height dependence in the  
176 hemispheric difference, but that SOFIE differences ( $\sim 65\%$  at  $0.1 \text{ hPa}$ ) are much larger than

177 WACCM (~12% at 0.1 hPa). The seasonal variation in smoke is largely driven by the global  
178 mesospheric meridional circulation, where the polar winter maximum is due to transport of smoke  
179 from across the globe. The larger hemispheric differences indicated by SOFIE could thus be the  
180 result of a stronger circulation in the NH winter (or weaker in SH winter) than is contained in the  
181 model. Another possibility is seasonal variability in the global meteoric input function. However,  
182 the variation that is currently in WACCM (based on dust sources at 1 AU in the solar system)  
183 indicates a symmetric distribution with respect to latitude and season [Feng *et al.*, 2013] because  
184 the Earth's orbit has a small eccentricity and inclination to the invariant plane of the solar system.  
185 At pressures lower than ~0.01 hPa, SOFIE results are increasingly affected by noise, and the NH  
186 - SH differences at these heights are not considered at this time. Examining smoke versus height  
187 in terms of volume density is relevant here because  $V$  is proportional to the retrieved extinction,  
188 which is in turn proportional to the measured signal. It is also useful to look at smoke in terms of  
189 mass mixing ratio (MMR) versus height, as is shown in Figure 3c. MMR is relevant because it  
190 illustrates that the relative abundance of smoke increases with height, which is a result of its  
191 extraterrestrial source. It is also useful when visualizing transport, because MMR is conserved  
192 during both horizontal and vertical advection.



194 Time series of the new SOFIE sunrise (NH) smoke volume densities are compared to  
 195 WACCM in Figure 4a, as the average  $V$  for 0.2 - 0.01 hPa ( $V'$ ). The SOFIE - WACCM agreement  
 196 is rather good, where both indicate similar annual variability and even a twin peak during winter.  
 197 The seasonal variation in smoke is shown in greater detail in Figure 4b, where the annual time  
 198 series are based on averages including 2007 - 2013. Recall that SOFIE smoke observations in  
 199 summer are generally not useful due to contamination by PMCs. The agreement is very good  
 200 concerning the timing and depth of the annual smoke variation, with the exception that WACCM  
 201 shows a later start to the autumn - winter enhancement than SOFIE. This difference is most likely  
 202 due to different timing of the seasonal transition in WACCM compared to the real atmosphere.



203

204           The year-to-year smoke variations were examined further using winter averages. The  
205 latitude of SOFIE observations in winter was consistently near  $\sim 70^\circ$  in both hemispheres, with the  
206 exception of 2017 - 2018 when lower latitudes were sampled due to the changing AIM orbit  
207 (Figure 5a). The comparison of smoke  $V'$  (Figure 5b) highlights the hemispheric asymmetry  
208 indicated by SOFIE (NH > SH), that is also present (although weaker) in WACCM (e.g., Figure  
209 3). The SOFIE NH observations show greater interannual variations than the SH measurements,  
210 which is consistent with greater variability in NH polar winter dynamics relative to the SH  
211 [*Schoeberl and Newman, 2015*]. WACCM also shows greater year-to-year variability in the NH  
212 compared to the SH, although variability in SOFIE is typically greater than in the model. Some of  
213 the interannual variability is due to the changing SOFIE latitudes after 2017, and this is captured  
214 in WACCM because the model was sampled to the SOFIE latitude vs. time. It is noteworthy,  
215 however, that SOFIE indicates more smoke in the NH not only during 2007 - 2018 when the NH  
216 was observed by sunrise occultations, but also in later years when the NH was observed by sunsets.  
217 This suggests that the hemispheric asymmetry is not due to a bias between the sunrise and sunset  
218 operational modes in SOFIE, but rather is a real characteristic of smoke in the polar mesosphere.

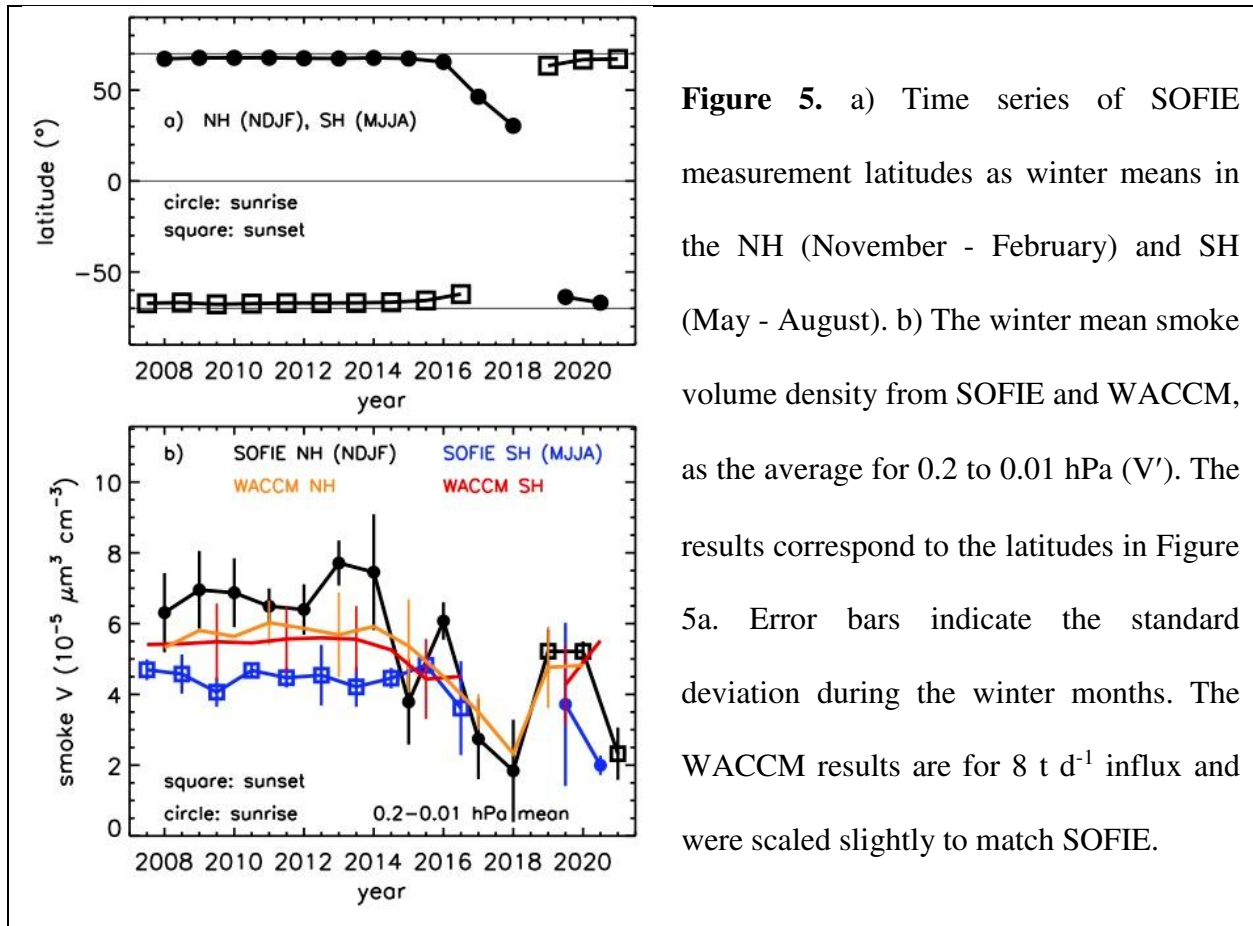
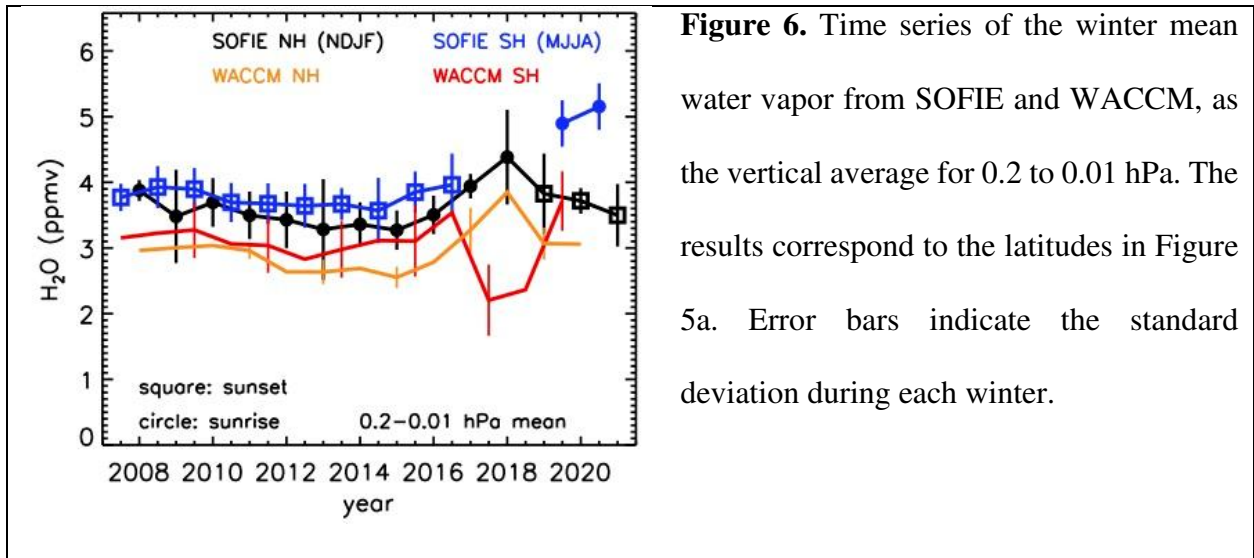


**Figure 5.** a) Time series of SOFIE measurement latitudes as winter means in the NH (November - February) and SH (May - August). b) The winter mean smoke volume density from SOFIE and WACCM, as the average for 0.2 to 0.01 hPa ( $V'$ ). The results correspond to the latitudes in Figure 5a. Error bars indicate the standard deviation during the winter months. The WACCM results are for  $8 \text{ t d}^{-1}$  influx and were scaled slightly to match SOFIE.

219

220 The hemispheric difference in smoke was further explored by looking at water vapor in the  
 221 upper mesosphere. Because  $\text{H}_2\text{O}$  behaves as a transport tracer and has a sharp vertical gradient in  
 222 the mesosphere, it could indicate hemispheric differences that can confirm those in meteoric  
 223 smoke. SOFIE and WACCM  $\text{H}_2\text{O}$  were examined as winter means in the upper mesosphere (0.2 -  
 224 0.01 hPa average, as for smoke). The results (Figure 6) show that there is less  $\text{H}_2\text{O}$  in the NH polar  
 225 winter than in the SH polar winter, in both SOFIE and WACCM. *Lossow et al.* [2009] were the  
 226 first to observe this hemispheric asymmetry in water vapor, and speculated that the underlying  
 227 cause was differences in dynamics and diffusion. Water vapor decreases with height to very low  
 228 values near the mesopause, so that descending air in the polar winter mesosphere causes seasonally  
 229 low  $\text{H}_2\text{O}$  [*Orsolini et al.*, 2010]. The hemispheric difference in winter  $\text{H}_2\text{O}$  is therefore suggestive

230 of stronger winter descent in the NH than the SH. This difference is qualitatively consistent with  
 231 the hemispheric differences in smoke volume density (Figure 5b), where more smoke in the NH  
 232 winter compared to the SH is indicative of stronger transport in the NH. Recall that the polar winter  
 233 increase in smoke is due to meridional transport, in addition to descent from meteoric ablation  
 234 heights (e.g., smoke MMR increases with height; Figure 3c). Note that SOFIE and WACCM agree  
 235 on the hemispheric differences in winter H<sub>2</sub>O (SH is ~10% > NH), but that the magnitude of the  
 236 hemispheric differences in smoke are much larger in SOFIE (20 to 80%) than in WACCM (<10%)  
 237 (Figure 5b). Nevertheless, it is too simplistic to infer a one-to-one correspondence between  
 238 different tracer profiles and pure advective transport, as noted by *Ryan et al.* [2018]. Other factors  
 239 such as chemistry or diffusion need to be considered [*Smith et al.*, 2011], and it is reasonable to  
 240 assume that these would behave differently for smoke and H<sub>2</sub>O. Differences in any one of these  
 241 factors between WACCM and the observations could explain the differences in the smoke and  
 242 H<sub>2</sub>O hemispheric asymmetries that are detected at polar latitudes.





## 243 **5. Meteoric Influx**

244 Ablated meteoric influx (AMI) was derived through comparisons of SOFIE smoke volume  
245 density with WACCM runs conducted for different AMI values, as discussed in detail by *Hervig*  
246 *et al.* [2017a]. WACCM shows that when AMI is changed, smoke  $V$  changes by nearly the same  
247 fractional amount at heights throughout the mesosphere. This is illustrated in Figures 7a - 7b,  
248 where the modeled  $V'$  (average  $V$  for 0.2 - 0.01 hPa) is shown versus month and latitude from  
249 WACCM runs with different AMI. The approach determines AMI vs.  $V'$  based on linear regression  
250 to the model results,  $AMI = A + B V'$ , where  $A$  should be zero. WACCM results for AMI = 2, 8,  
251 and  $11 \text{ t d}^{-1}$  were used in the regressions (Figures 7a and 7b), with the additional constraint that  
252 the point ( $V' = 0$ , AMI = 0) was included to encourage  $A$  to approach zero. Values of  $A$  have only  
253 small departures from zero ( $< 3\%$ ), which reflect the uncertainties in the approach (not shown).  
254 Because the SOFIE latitudes have changed over time (Figure 1), the regression to WACCM results  
255 was carried out for monthly zonal means over a complete range in latitude. Values of  $B$  at polar  
256 latitudes are found to change dramatically with season, with similar values during winter in both  
257 hemispheres (Figures 7c - 7d). High values of  $B$  in summer occur because smoke is depleted due  
258 to transport by the meridional circulation, while the regression was to the same annual global mean  
259 AMI values. The results are also found to vary with latitude (Figure 7d), where the variation is  
260 again driven by smoke transport.

261 The uncertainties in derived influx are a combination of the SOFIE observational errors  
262 ( $\sim 9\%$  for monthly means), and the statistical uncertainty in the WACCM representation of  $V'$  vs.  
263 AMI ( $\sim 3\%$  in polar winter). The AMI uncertainties ( $\delta AMI$ ) are the root-sum-square of these terms,  
264 and the average  $\delta AMI$  for either hemisphere is  $\sim 10\%$  during 2007 - 2021. Recall also that the  
265 SOFIE  $V$  and influx values are based on that assumption that smoke is composed of Fe-rich

266 olivine. While this assumption is justified in numerous ways, the ramifications of considering other  
 267 smoke compositions are briefly considered. Previous SOFIE results indicate various smoke  
 268 compositions, and an alternate approach here would be to consider the mean optical characteristics  
 269 for the range of compositions, as was done in *Hervig et al.* [2017a] (see also Section 2). Taking  
 270 that approach would cause a ~45% reduction in smoke V, and the subsequently derived AMI. In  
 271 addition, the resulting V and AMI uncertainties would increase from ~10% to ~55%, due to the  
 272 variability in optical properties for the different smoke compositions. Nevertheless, the results here  
 273 are supportive of smoke existing as Fe-rich olivine, and we proceed under that assumption.  
 274

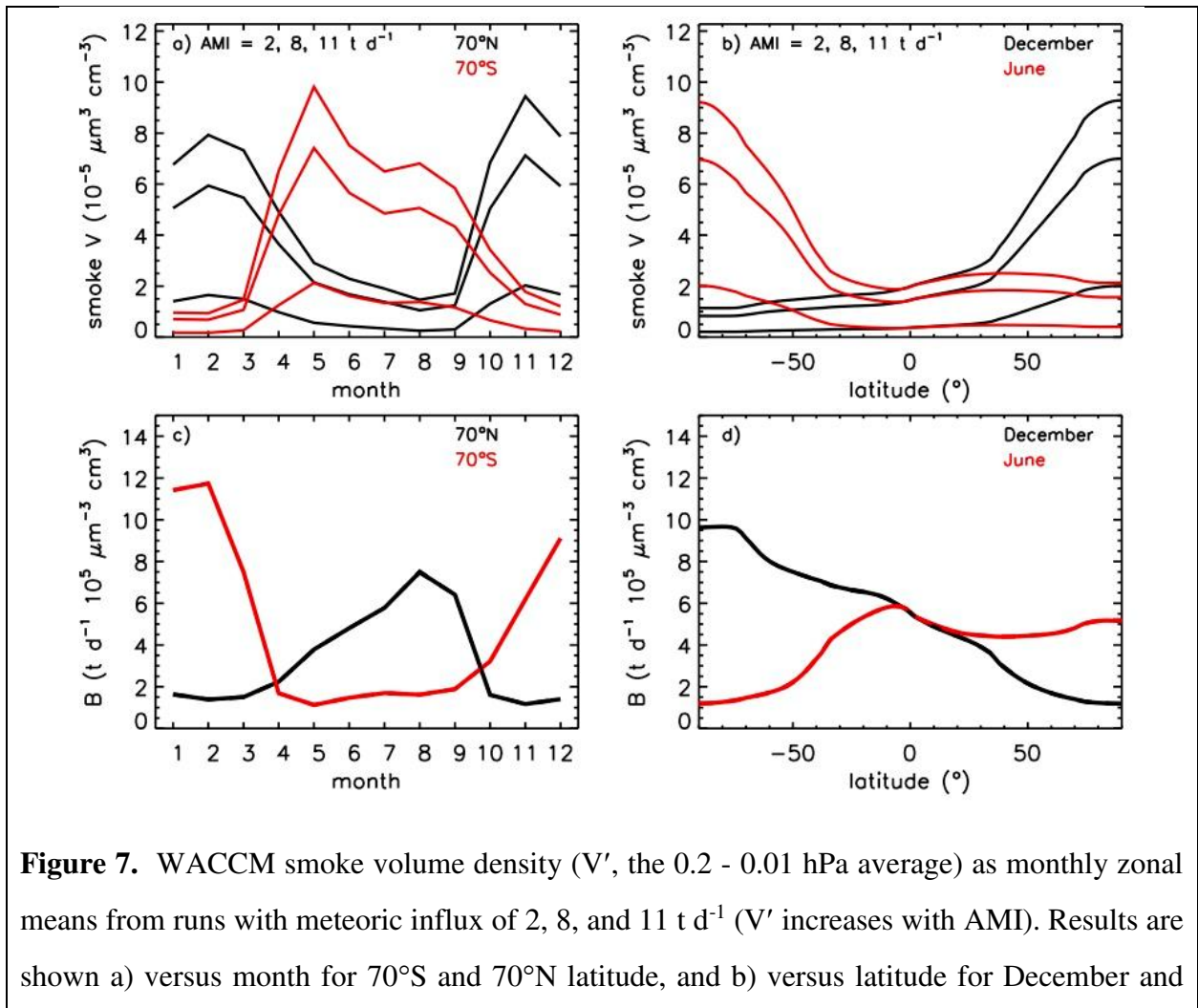


**Figure 7.** WACCM smoke volume density ( $V'$ , the 0.2 - 0.01 hPa average) as monthly zonal means from runs with meteoric influx of 2, 8, and 11  $\text{t d}^{-1}$  ( $V'$  increases with AMI). Results are shown a) versus month for 70°S and 70°N latitude, and b) versus latitude for December and

June. The slope ( $B$ ) for linear regression to WACCM AMI versus  $V'$  is shown c) versus month at  $70^{\circ}\text{S}$  and  $70^{\circ}\text{N}$ , and d) versus latitude for December and June.  $B$  was determined from monthly zonal means for 2007 - 2015 (before the SOFIE orbit changed). Uncertainties in  $B$  during high latitude winter are  $\sim 3\%$ .

275

276 Ablated influx is shown versus month in Figure 8 during autumn through spring when  
277 meteoric smoke is most abundant (e.g., Figure 4b). The AMI estimates have additional errors  
278 during the transitional months when the SOFIE - WACCM agreement is poorer (e.g., September  
279 in the NH, see Figure 4b), although this is not captured in the current uncertainty estimates. Recall  
280 also that SOFIE smoke observations are typically not obtained in high latitude summer due to  
281 signal contamination by PMCs. The results in Figure 8 are for 2007 - 2017 when sunrise (sunset)  
282 was in the NH (SH). The average NH AMI is  $\sim 30\%$  greater than for the SH, which is statistically  
283 significant in terms of the AMI uncertainties ( $\sim 10\%$ ). If SOFIE and WACCM contained the exact  
284 same seasonal variation in mesospheric smoke, however, then the AMI derived here should be  
285 constant throughout the year (by definition). Thus, the monthly variations in AMI can be  
286 interpreted as a byproduct of SOFIE - WACCM differences in the seasonal variation of smoke, as  
287 apparent in Figure 4b. The best AMI estimates from the SOFIE - WACCM comparisons will  
288 therefore be from multi-month averages, preferably during winter when smoke is elevated and  
289 relatively stable in time.

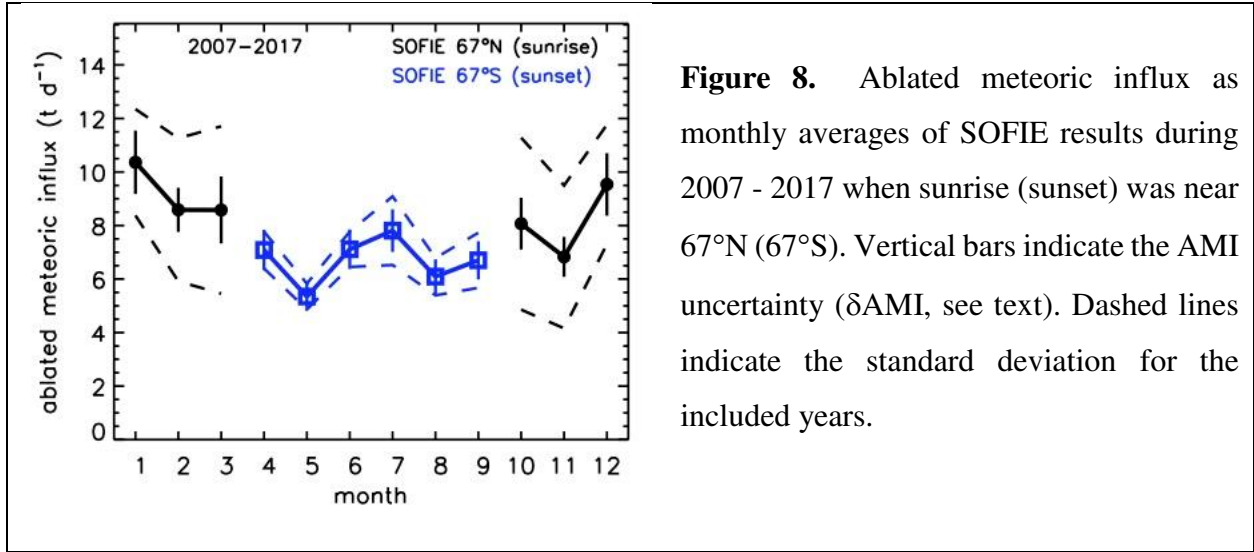


**Figure 8.** Ablated meteoric influx as monthly averages of SOFIE results during 2007 - 2017 when sunrise (sunset) was near 67°N (67°S). Vertical bars indicate the AMI uncertainty ( $\delta$ AMI, see text). Dashed lines indicate the standard deviation for the included years.

290

291 Ablated meteoric influx during 2007 - 2021 is shown as winter averages in both

292 hemispheres in Figure 9, where the results are mostly for polar latitudes. AMI in the NH is typically

293 greater than in the SH, with averages during 2007 - 2021 of  $8.4 \pm 2.0 \text{ t d}^{-1}$  in the NH, and  $6.2 \pm 1.4$

294  $\text{t d}^{-1}$  in the SH ( $\pm$  standard deviation of 14 years). For both hemispheres combined AMI is  $7.3 \pm$

295  $2.0 \text{ t d}^{-1}$ . The above standard deviations for 2007 - 2021 are  $\sim 22\%$ , while the AMI uncertainty

296 based on SOFIE and WACCM errors combined is  $\sim 10\%$ , for either hemisphere. The results

297 indicate inter-annual variations in meteoric influx that are often statistically significant. Other

298 observation of meteoric influx have shown year-to-year variability, including radars [e.g., *Janches*

299 *et al.*, 2004] and satellite instruments [*Malaspina et al.*, 2016]. It is thus possible that the SOFIE

300 inter-annual variations indicate real variability in meteoric influx, but this will be the topic of future

301 studies.

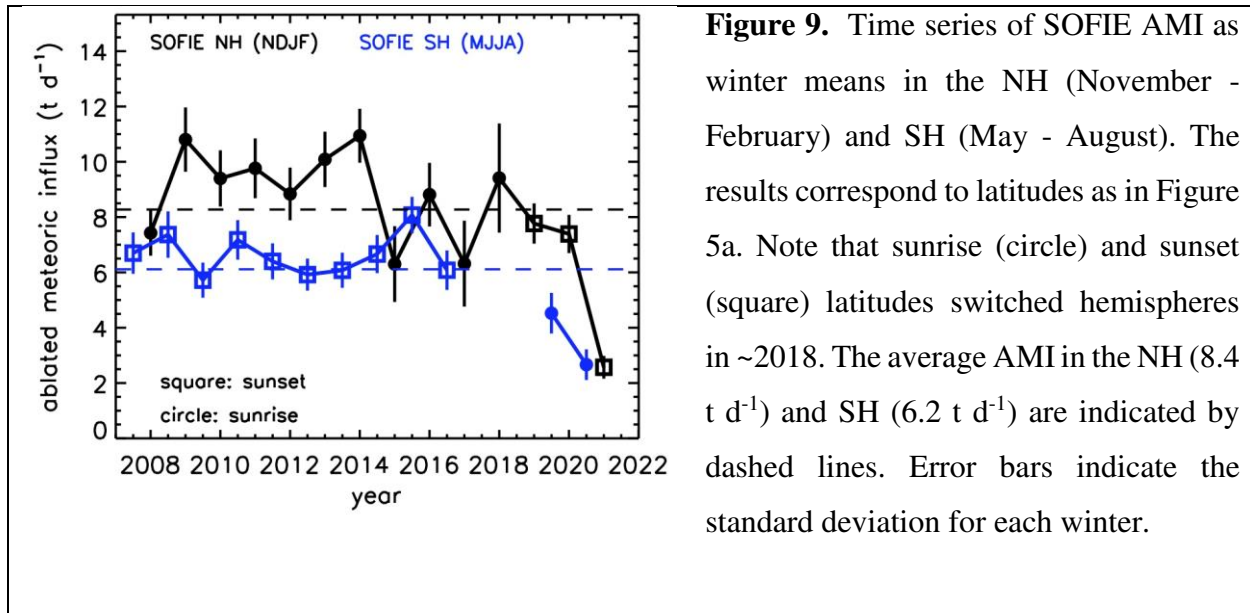


**Figure 9.** Time series of SOFIE AMI as winter means in the NH (November - February) and SH (May - August). The results correspond to latitudes as in Figure 5a. Note that sunrise (circle) and sunset (square) latitudes switched hemispheres in ~2018. The average AMI in the NH (8.4 t d<sup>-1</sup>) and SH (6.2 t d<sup>-1</sup>) are indicated by dashed lines. Error bars indicate the standard deviation for each winter.

302

303 The AMI derived here from the SOFIE-WACCM comparisons were anticipated to be equal

304 in both hemispheres, yet hemispheric differences (NH > SH) exist during most years (Figure 9).

305 This is due in part to hemispheric differences in SOFIE smoke volume density, that are weaker in

306 WACCM (Figure 5b). Indeed, if WACCM had the same hemispheric differences in smoke  $V'$  as

307 SOFIE, then the resulting AMI would be equal in both hemispheres. Biases between the SOFIE

308 sunrise and sunset observational modes were dismissed because the hemispheric difference

309 persists after 2018 when sunrise switched from the NH to SH (see Section 4). Transport in the

310 model was dismissed because hemispheric differences in SOFIE and WACCM wintertime

311 mesospheric H<sub>2</sub>O are similar (Section 4). Another explanation might be a hemispheric asymmetry

312 in the interaction of smoke with an atmospheric constituent which changes the optical properties

313 of the particles. The most likely candidate is H<sub>2</sub>SO<sub>4</sub>-H<sub>2</sub>O (sulfate) droplets in the mid-stratosphere,

314 since these can entrain smoke particles to produce sulfate droplets with a smoke core (*Brooke et*

315 *al.*, 2017). Dissolution of the Fe in smoke to form Fe<sup>2+</sup>/Fe<sup>3+</sup> ions in the droplets is rapid under

316 stratospheric conditions (~20 hrs. at 235 K, see *Saunders et al.*, 2012), and these droplets may have

317 different optical properties to pure smoke. The model results of *Brooke et al.* [2017] indicated that  
318 mixed smoke-sulfate particle formation should only be significant below 35 km. *Hervig et al.*  
319 [2017b], however, used SOFIE observations with models to show that when sulfuric acid is  
320 neutralized by mixing with smoke, that a sulfate-smoke aerosol can form at heights reaching into  
321 the lower mesosphere. In any case, sulfate - smoke interactions are not included in the present  
322 WACCM model runs and thus could be a candidate for the observed asymmetries. A final  
323 possibility is that the hemispheric difference in SOFIE smoke is due to an asymmetry in meteoric  
324 influx that is not included in WACCM. *Malaspina et al.* [2016] report meteoric flux observations  
325 from the Wind satellite operating roughly  $10^6$  km from Earth, showing a seasonal variation in MI  
326 with a maximum in March and a minimum in September. This annual variation was traced to  
327 interstellar particles, which flow into the Earth's orbital direction in March. While interstellar  
328 particles may comprise too little mass to explain the observed asymmetries, the question is posed  
329 here as there may be unexplored characteristics of the interstellar flow. The Wind dust observations  
330 are not considered in the *Fentzke et al.* [2008] description of meteoric influx variations used in  
331 WACCM, and thus could be a component in the SOFIE - WACCM disagreement concerning the  
332 hemispheric differences in mesospheric smoke.

333         The final consideration is derivation of total meteoric influx (TMI) from the SOFIE ablated  
334 meteoric influx results. The present study treats meteoric smoke as Fe-rich olivine, which has an  
335 elemental abundance nearly identical to that of the ablated meteoric source (see Section 2). As a  
336 result, the conversion from AMI to TMI can be taken directly from the *Carrillo-Sánchez et al.*  
337 [2020] results, which give  $\text{TMI} / \text{AMI} = 28 \pm 16 \text{ t d}^{-1} / 8.3 \pm 4.7 \text{ t d}^{-1} = 3.4$ . The resulting TMI  
338 values from this work are  $28.4 \pm 6.8 \text{ t d}^{-1}$  in the NH and  $21.0 \pm 4.9 \text{ t d}^{-1}$  in the SH. For both  
339 hemispheres combined TMI is  $25.0 \pm 7.0 \text{ t d}^{-1}$ . The stated uncertainties are the standard deviation

340 of the winter values for 2007 - 2021 (e.g., Figure 9). Note that uncertainties in the SOFIE TMI  
341 estimates reported above are the standard deviations over 14 years, and that the experimental errors  
342 represent an additional 10% uncertainty. It is furthermore arguable that the SOFIE TMI  
343 uncertainties could be increased due to propagation of the *Carrillo-Sánchez et al.* [2020] errors  
344 (~57%).

## 345 **6. Summary**

346 An improved SOFIE sunrise signal calibration has produced meteoric smoke extinction  
347 retrievals in the Northern Hemisphere, for the first time. The new observations are in good  
348 agreement with WACCM simulations concerning both the time and height dependence of smoke  
349 in the mesosphere. Comparing the SOFIE extinction measurements to WACCM requires  
350 knowledge of the smoke composition, to describe the optical properties that relate extinction to  
351 volume density. The present study assumes that smoke in the mesosphere exists purely as Fe-rich  
352 olivine ( $\text{Mg}_{0.8}\text{Fe}_{1.2}\text{SiO}_4$ ) with the justification that 1) it is detected optically by SOFIE [*Hervig et*  
353 *al.*, 2017a], 2) it has the same elemental abundance of Fe, Mg and Si as predicted from meteoric  
354 ablation, and 3) it is anticipated by theory and laboratory experiments [*Saunders and Plane*, 2011].  
355 With the assumption of olivine, SOFIE results indicate a global mean ablated meteoric influx of  
356  $7.3 \pm 2.0 \text{ t d}^{-1}$  (total influx of  $25.0 \pm 7.0 \text{ t d}^{-1}$ ), based on averages for both hemispheres during 2007  
357 - 2021. The new SOFIE influx results agree with *Carrillo-Sánchez et al.* [2020] (within 11%) who  
358 used models and observations to derive an ablated influx of  $8.3 \pm 4.7 \text{ t d}^{-1}$  (total influx of  $28.0 \pm$   
359  $16 \text{ t d}^{-1}$ ). This closure provides further support for mesospheric smoke existing as olivine.  
360 Additionally, these new results reconcile previous differences between SOFIE influx estimates  
361 from *Hervig et al.* [2017a] (AMI =  $3.3 \text{ t d}^{-1}$ ; TMI =  $30 \text{ t d}^{-1}$ ) and *Carrillo-Sánchez et al.* [2016]  
362 (AMI =  $7.9 \text{ t d}^{-1}$ ; TMI =  $43 \text{ t d}^{-1}$ ).

363 Both SOFIE and WACCM show ~10% hemispheric differences in wintertime mesospheric  
364 H<sub>2</sub>O (SH > NH), that are consistent with stronger transport in the NH winter vs. the SH. This  
365 difference in transport is also apparent in both the SOFIE and WACCM mesospheric smoke  
366 results, which show less smoke in the SH polar winter compared to NH winter. The open issue is  
367 that the hemispheric smoke difference is greater in SOFIE (~36%) than in WACCM (~2%).  
368 Because the meteoric influx estimates rely on comparisons of SOFIE and WACCM, a hemispheric  
369 difference emerges in the SOFIE influx values (~30%). While this difference is close to the  
370 combination of experimental uncertainties (~10%) and geophysical variability during the 14 years  
371 of observations (~20%), it is persistent in time and bears some thought. Sunrise - sunset biases in  
372 the SOFIE observations were dismissed because the hemispheric difference persists after 2018  
373 when sunrise switched from the NH to SH (vice versa for sunset). Transport in WACCM was  
374 dismissed because the hemispheric differences in H<sub>2</sub>O are the same in WACCM and SOFIE. The  
375 parting ideas in this regard are incomplete chemistry or microphysics in the smoke simulations, or  
376 asymmetries in meteoric influx that are not represented in the model.

377 **Acknowledgements.** This work was funded in part by the AIM mission through NASA's Small  
378 Explorers Program under contract NAS5-03132. The modeling work at the University of Leeds  
379 was supported by the European Research Council (project number 291332 – CODITA). SOFIE  
380 data are available online at [sofie.gats-inc.com](http://sofie.gats-inc.com). The updated SOFIE extinctions used in this study  
381 are available by contacting Mark Hervig ([mark@gats-inc.com](mailto:mark@gats-inc.com)). The WACCM data sets generated  
382 for this work have been archived at the University of Leeds  
383 (<http://doi.org/10.5281/zenodo.4893548>).

## 384 **References**

385 Bardeen, C. G., O. B. Toon, E. J. Jensen, D. R. Marsh, and V. L. Harvey (2008), Numerical



386 simulations of the three-dimensional distribution of meteoric dust in the mesosphere and upper  
387 stratosphere, *J. Geophys. Res.*, *113*, D17202, doi:10.1029/2007JD009515.

388 Bardeen, C. G., O. B. Toon, E. J. Jensen, M. E. Hervig, C. E. Randall, S. Benze, D. R. Marsh, and  
389 A. Merkel (2010), Numerical simulations of the three-dimensional distribution of polar  
390 mesospheric clouds and comparisons with Cloud Imaging and Particle Size (CIPS)  
391 experiment and the Solar Occultation For Ice Experiment (SOFIE) observations, *J. Geophys.*  
392 *Res.*, *115*, D10204, doi:10.1029/2009JD012451.

393 Brooke, J. S. A., Feng, W., Carrillo-Sánchez, J. D., Mann, G. W., James, A. D., Bardeen, C. G.,  
394 Marshall, L., Dhomse, S. S., & Plane, J. M. C. (2017). Meteoric smoke deposition in the polar  
395 regions: A comparison of measurements with global atmospheric models. *J. Geophys. Res.*  
396 *Atm.*, *122*, 11,112– 11,130. <https://doi.org/10.1002/2017JD027143>.

397 Carrillo-Sánchez, J. D., D. Nesvorný, P. Pokorný, D. Janches, and J. M. C. Plane (2016), Sources  
398 of cosmic dust in the Earth's atmosphere, *Geophys. Res. Lett.*, *43*,  
399 doi:10.1002/2016GL071697.

400 Carrillo-Sánchez, J. D.; Gómez-Martín, J. C.; Bones, D. L.; Nesvorný, D.; Pokorný, P. Benna, M.;  
401 Flynn, G. F.; Plane, J. M. C. (2020) Cosmic dust fluxes in the atmospheres of Earth, Mars,  
402 and Venus, *Icarus*, *335*, art. no. 113395.

403 Feng, W., Marsh, D. R., Chipperfield, M. P., Janches, D., Hoffner, J. Yi, F., and Plane, J. M. C.  
404 (2013): A global atmospheric model of meteoric iron, *Journal of Geophysical Research*, *118*,  
405 9456–9474.

406 Fentzke, J.T., D. Janches, and J.J. Sparks (2008), Latitudinal and seasonal variability of the  
407 micrometeor input function: A study using model predictions and observations from Arecibo

408 and PFISR, *J. Atmos. Solar-Terr. Phys.*, doi:10.1016/j.jastp.2008.07.015.

409 Frankland, V. L.; James, A. D.; Feng, W.; Plane, J. M. C. (2015): The uptake of HNO<sub>3</sub> on meteoric  
410 smoke analogues, *Journal of Atmospheric and Solar-Terrestrial Physics*, 127, 150-160, 127,  
411 150-160, doi: 10.1016/j.jastp.2015.01.010.

412 Gardner, C. S., Alan Z. Liu, D. R. Marsh, Wuhu Feng and J. M. C. Plane (2014), Inferring the  
413 Global Cosmic Dust Influx to the Earth's Atmosphere from Lidar Observations of the Vertical  
414 Flux of Mesospheric Na, *J. Geophys. Res. Space Physics*, DOI: 10.1002/2014JA020383.

415 Gordley, L. L., et al. (2009), The Solar Occultation For Ice Experiment (SOFIE), *J. Atmos. Sol.-*  
416 *Terr. Phys.*, 71, 300-315, doi:10.1016/j.jastp.2008.07.012.

417 Gelaro, R., McCarty, W., Suárez, M. J., Todling, R., Molod, A., Takacs, L., Randles, C. A.,  
418 Darmenov, A., Bosilovich, M. G., Reichle, R., Wargan, K., Coy, L., Cullather, R., Draper, C.,  
419 Akella, S., Buchard, V., Conaty, A., da Silva, A. M., Gu, W., Kim, G., Koster, R., Lucchesi,  
420 R., Merkova, D., Nielsen, J. E., Partyka, G., Pawson, S., Putman, W., Rienecker, M., Schubert,  
421 S. D., Sienkiewicz, M., & Zhao, B. (2017). The Modern-Era Retrospective Analysis for  
422 Research and Applications, Version 2 (MERRA-2), *Journal of Climate*, 30(14), 5419-5454,  
423 <https://journals.ametsoc.org/view/journals/clim/30/14/jcli-d-16-0758.1.xml>.

424 Hervig, M. E., L. L. Gordley, L. E. Deaver, D. E. Siskind, M. H. Stevens, J. M. Russell III, S. M.  
425 Bailey, L. Megner, and C. G. Bardeen (2009), First satellite observations of meteoric smoke  
426 in the middle atmosphere, *Geophys. Res. Letters*, doi:10.1029/2009GL039737.

427 Hervig, M. E., Brooke, J. S. A., Feng, W., Bardeen, C. G., Plane, J. M. C. (2017a), Constraints on  
428 meteoric smoke composition and meteoric influx using SOFIE observations with models, *J.*  
429 *Geophys. Res. Atmospheres*, 122, doi:10.1002/2017JD027657.

430 Hervig, M. E., C. G. Bardeen, D. E. Siskind, M. J. Mills, R. Stockwell, (2017b), Meteoric smoke

431 and H<sub>2</sub>SO<sub>4</sub> aerosols in the upper stratosphere and mesosphere, *Geophys. Res. Letters*, 44,  
432 doi:10.1002/2016GL072049.

433 James, A. D., D. R. Moon, W. Feng, P. S. J. Lakey, V. L. Frankland, D. E. Heard, J. M. C. Plane  
434 (2017), The uptake of HO<sub>2</sub> on meteoric smoke analogues, *J. Geophys. Res.*, 122, 554–565.

435 Janches, D., S. Palo, E. M. Lau, S. K. Avery, J. P. Avery. S. de la Peña, N. A. Makarov (2004),  
436 Diurnal and seasonal variability of the meteor flux at the South Pole measured with radars,  
437 *Geophys. Res. Lett.*, 31, doi:10.1029/2004GL021104.

438 Lossow, S., J. Urban, H. Schmidt, D. R. Marsh, J. Gumbel, P. Eriksson, and D. Murtagh (2009),  
439 Wintertime water vapor in the polar upper mesosphere and lower thermosphere: First satellite  
440 observations by Odin submillimeter radiometer, *J. Geophys. Res.*, 114, D10304,  
441 doi:10.1029/2008JD011462.

442 Malaspina, D. M. and L. B. Wilson III (2016), A database of interplanetary and interstellar dust  
443 detected by the Wind spacecraft, *J. Geophys. Res. Space Physics*, 121, 9369–9377,  
444 doi:10.1002/2016JA023209.

445 Marsh, D. R., Janches, D., Feng, W. and Plane, J. M. C. (2013a): A global model of meteoric  
446 sodium, *J. Geophysical Research*, 118, 11,442–11,452.

447 Marsh, D. R., M. J. Mills, D. E. Kinnison, J. F. Lamarque, N. Calvo, and L. M. Polvani (2013b),  
448 Climate Change from 1850 to 2005 Simulated in CESM1(WACCM), *J. Clim.*, 26, 7372-7391.

449 Megner, L, D. E. Siskind, M. Rapp, and J. Gumbel (2008), Global and temporal distribution of  
450 meteoric smoke; a 2D simulation study, *J. Geophys. Res.*, 113, D03202,  
451 doi:10.1029/2007JD009054.

452 Molod, A., Takacs, L., Suarez, M., and Bacmeister, J.: Development of the GEOS-5 atmospheric  
453 general circulation model: evolution from MERRA to MERRA2, *Geosci. Model Dev.*, 8,

454 1339–1356, <https://doi.org/10.5194/gmd-8-1339-2015>, 2015.

455 Orsolini, Y. J., Urban, J., Murtagh, D. P., Lossow, S., and Limpasuvan, V. (2010), Descent from  
456 the polar mesosphere and anomalously high stratopause observed in 8 years of water vapor  
457 and temperature satellite observations by the Odin Sub-Millimeter Radiometer, *J. Geophys.*  
458 *Res.*, *115*, D12305, doi:10.1029/2009JD013501.

459 Plane, J. M. C. (2012), Cosmic dust in the earth’s atmosphere, *Chem. Soc. Rev.*, *41*, 6507-6518,  
460 doi: 10.1039/c2cs35132c.

461 Plane, J. M. C., W. Feng; Dawkins, E. C. M. (2015): The Mesosphere and Metals: Chemistry and  
462 Changes, *Chemical Reviews*, *115*, 4497 - 4541, doi: 10.1021/cr500501m.

463 Russell, J. M. III, et al. (2009), Aeronomy of Ice in the Mesosphere (AIM): Overview and early  
464 science results, *J. Atmos. Sol.-Terr. Phys.*, *71*, 289-299, doi:10.1016/j.jastp.2008.08.011.

465 Ryan, N. J., Kinnison, D. E., Garcia, R. R., Hoffmann, C. G., Palm, M., Raffalski, U., and Notholt,  
466 J. (2018): Assessing the ability to derive rates of polar middle-atmospheric descent using trace  
467 gas measurements from remote sensors, *Atmos. Chem. Phys.*, *18*, 1457–1474,  
468 <https://doi.org/10.5194/acp-18-1457-2018>.

469 Saunders, R.W. and J. M. Plane (2011), A photo-chemical method for the production of olivine  
470 nanoparticles as cosmic dust analogues, *Icarus*, *212*, 373-382, ISSN 0019-1035,  
471 [10.1016/j.icarus.2010.12.019](https://doi.org/10.1016/j.icarus.2010.12.019).

472 Saunders, R. W., S. Dhomse, W. S. Tian, M. P. Chipperfield, and J. M. C. Plane (2012),  
473 Interactions of meteoric smoke particles with sulphuric acid in the Earth’s stratosphere, *Atmos.*  
474 *Chem. Phys.*, *12*, 4387–4398, doi:10.5194/acp-12-4387-2012.

475 Schoeberl, M.R., and P.A. Newman (2015), Encyclopedia of Atmospheric Sciences (Second  
476 Edition), *Academic Press*, 2015, Pgs 12-17, ISBN 9780123822253,

477 <https://doi.org/10.1016/B978-0-12-382225-3.00228-0>.

478 Smith, A. K., R. R. Garcia, D. R. Marsh, and J. H. Richter (2011), WACCM simulations of the  
479 mean circulation and trace species transport in the winter mesosphere, *J. Geophys. Res.*, *116*,  
480 D20115, doi:10.1029/2011JD016083.

481 Vondrak, T., J. M. C. Plane, S. Broadley, and D. Janches (2008), A chemical model of meteoric  
482 ablation, *Atmospheric Chemistry and Physics*, *8* (23), 7015-7031.